

# Computer simulation of strain accumulation and hardening for pearlitic rail steel undergoing repeated contact

A Kapoor\*, J H Beynon, D I Fletcher and M Loo-Morrey  
Department of Mechanical Engineering, University of Sheffield, UK

**Abstract:** This paper presents a validated model of plastic strain accumulation in railway rail steel under repeated wheel–rail contact. Such contacts subject the rails to severe stresses, taking the material local to the contact beyond yield, and leading to the incremental accumulation of plastic deformation (ratcheting) as wheels pass. This process is at the root of several rail wear and rolling contact fatigue crack growth mechanisms. Existing plasticity models are inadequate for modelling the strain accumulation taking place in this material, which is under high hydrostatic compression (of the order of 1 GPa) and is severely anisotropic. The model described here is based on a ratcheting law derived from small-scale twin-disc rolling–sliding contact experiments and simulates tens of thousands of ratcheting cycles and the corresponding strain hardening in a few minutes on a personal computer. Results indicate that, to model these processes successfully, and to represent correctly the high levels of ductility seen in rail steels under compressive load, stress–strain data generated under high hydrostatic compression are required.

**Keywords:** hydrostatic, pearlitic, steel, rail, ratcheting, simulation

## 1 INTRODUCTION

### 1.1 Background

Railway wheel–rail contacts subject rails to severe stresses, taking the material local to the contact beyond yield in a state approaching hydrostatic compression, leading to the incremental accumulation of plastic deformation (ratcheting) as wheels pass. This accumulation of plastic deformation is at the root of several wear and rolling contact fatigue crack growth mechanisms which affect rails. Its understanding is therefore critical to the safe operation of the railway, and to the planning of rail maintenance and renewal. Track renewals (excluding maintenance) cost £913 million for Network Rail in the United Kingdom during the financial year 2002–2003 [1], representing a large proportion of the cost of railway operations. To increase understanding of the problem this paper presents a model describing plastic strain accumulation in railway rail steel under repeated contact.

The model described in this paper is designed to form an input to higher-level models of rail wear and fatigue. Wear through loss of material which has undergone ratcheting to the point at which its ductility is exhausted is being investigated by Kapoor and Franklin [2]. The work of Kapoor and Franklin is distinguished from previous ratcheting wear modelling by the inclusion of material property variation on the micron scale. Investigation of crack initiation through ductility exhaustion is also taking place using an image analysis technique to identify cracks (i.e. contiguous regions of exhausted material) in a graphical representation of a deformed material [3].

A recent development through which the influence of ratcheting on rail life can be investigated is the whole life rail model (WLRM) [4, 5] which has brought together in one model predictions of wear, crack initiation and crack propagation attributable to both contact stress and rail bending stresses. Ratcheting influences wear and crack initiation, and the WLRM emphasizes the way in which these processes interact with crack propagation to control rail life. Early results from the model show good correspondence to field behaviour of rails; however, the outcomes of such models depend critically on the input data for each rail degradation process.

For a model of plastic strain accumulation to form a useful input to the models described above, and therefore

*The MS was received on 17 June 2003 and was accepted after revision for publication on 16 October 2003.*

*\*Corresponding author: Department of Mechanical Engineering, University of Sheffield, Frederick Mappin Building, Mappin Street, Sheffield S1 3JD, UK.*

to be of use in the railway industry, it needs to be capable of considering the wide variety of conditions to which a single section of rail may be subjected during its life. It also needs to be capable of simulating many thousands of contact cycles in a short amount of time (minutes) and should require a minimum of input data, so that the vast variety of contact conditions and materials present across the rail network can be investigated. For these reasons a simplistic empirical modelling approach is taken here, based on the outcomes of twin-disc materials testing. This is in contrast to alternative models of strain accumulation based on plasticity theory such as those by Armstrong and Frederick [6], Jiang and Sehitoglu [7, 8], Lemaitre and Chaboche [9] and Ringsberg *et al.* [10, 11]. These models typically have long run times (days rather than minutes when implemented using the finite element code for failure over thousands of load cycles) and in the case of the work by Jiang and Sehitoglu require many material parameters, which are unlikely to be available in a railway industry context. In addition, validation of models based on plasticity theory with the deformation seen following rolling–sliding contact loading is uncommon because rolling–sliding contact typically involves non-proportional loading cycles, highly anisotropic materials and high hydrostatic compression (typically of the order of 1 GPa). The empirical model described here is validated using data from twin-disc tests on pearlitic rail steel conducted by Tyfour *et al.* [12] under rolling–sliding contact conditions characteristic of rail–wheel contact.

## 1.2 Rail–wheel contact conditions and material response

Axle loads up to 25 t which are typically seen in the railway industry [13] result in contact pressures many times those at which yield of the rail material takes place. Expressed as maximum Hertzian contact pressures [14] rail–wheel contacts can reach 830–3000 MPa, depending on contact patch location, dynamic loading and vehicle type [15]. This high normal pressure is typically combined with shear stresses when wheels are driving or braking or when the vehicle is cornering, with traction coefficients (traction force divided by normal load) in the range 0.2–0.6 depending on conditions [16, 17]. If it is assumed that the contact is fully sliding, then this traction coefficient is equal to the friction coefficient at the rail–wheel interface.

Ratcheting (the incremental accumulation of plastic strain in an open strain loop) is the typical response of a material to this cyclic loading. The process is illustrated in Fig. 1, and occurs when the maximum Hertzian contact pressure exceeds the shakedown limit, as shown in Fig. 1. The stress driving plastic deformation in ratcheting is determined by how far the shakedown limit is exceeded but, even when the region close to the rail–wheel contact is taken beyond this limit, the deformation

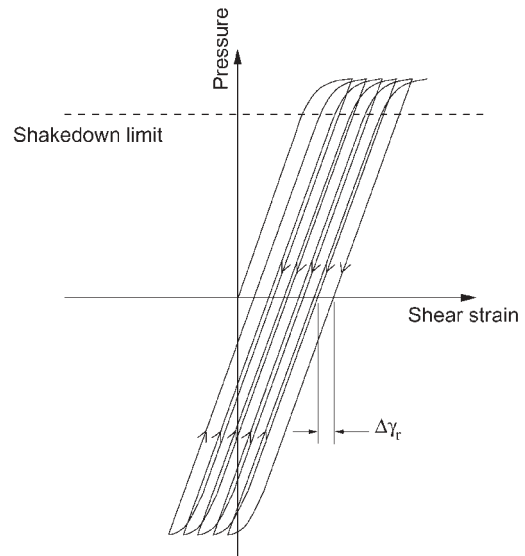


**Fig. 1** Pressure versus displacement for a body repeatedly loaded above the plastic shakedown limit. Ratcheting (accumulation of increments of plastic strain with each loading) gives the characteristic looped appearance to the plot, representing the increase in plastic deformation with each pressure application [18].  $\Delta\gamma_r$  is the ratcheting component of the strain cycle

is constrained by surrounding material which is less heavily loaded. The increment of plastic deformation in 1 cycle is therefore of the order of the elastic yield strain but, although this strain is low, over thousands of wheel passes these increments of deformation accumulate and the total deformation can far exceed the elastic yield strain. As ratcheting takes place, failure occurs when the plastic strain accumulated by the material reaches a limit beyond which the material loses its integrity and fails. The plastic strain  $\gamma_c$  at this point is known as the limiting ductility, or critical failure strain of the material, and is a quantity that must be determined experimentally. The failure process is often referred to as ductility exhaustion, and the number  $N_r$  of cycles before failure can be determined from the ratcheting component of the strain cycle ( $\Delta\gamma_r$ , illustrated in Fig. 1) and the critical failure strain of the material [18]:

$$N = \frac{\gamma_c}{\Delta\gamma_r} \quad (1)$$

Low-cycle fatigue, which is relevant to a closed cycle of plastic strain, is not considered here because twin-disc rolling contact tests including reversal of rolling direction [19] indicate that ratcheting rather than low-cycle fatigue is appropriate to describe failure of rail steel under the conditions that it experiences in service.

## 1.3 Experimental data

Tyfour *et al.* [12] conducted a series of twin-disc rolling–sliding contact tests on BS11 normal-grade pearlitic rail

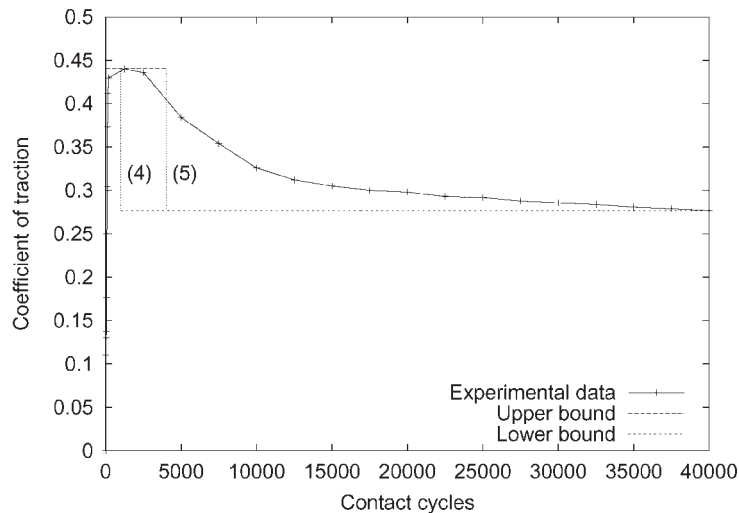


**Fig. 2** Traction coefficient versus number of contact cycles for a 40 000 cycle dry twin-disc test conducted by Tyfour *et al.* [12] on pearlitic rail steel. Upper- and lower-bound friction coefficient lines are joined by lines (4) and (5), indicating the friction coefficients applied in simulations 4 and 5 (1000 and 4000 upper bound cycles respectively)

steel using a laboratory-based simulation machine [20, 21]. Tests were conducted under dry conditions; therefore failure was attributable primarily to ratcheting. Complications such as fluid-assisted crack growth which can affect rails in service [22] were avoided. The tests were conducted using discs of 47 mm diameter at a maximum Hertzian contact pressure of 1500 MPa. To simulate a driving wheel, slip was introduced between the discs by giving them a 1 per cent difference in surface speed. Following the tests the rail discs were sectioned and prepared for examination using standard metallographic techniques. The traction coefficient was measured during the tests giving the results plotted in Fig. 2, and following testing hardness was measured at a range of depths from just below the surface to 1.6 mm deep (the hardness varied because the material was strain hardening). The accumulated shear strain was measured 0.2 mm below the surface using the technique shown in Fig. 3. This was the shallowest depth at which reliable measurements could be taken because above this point the integrity of the surface was lost owing to ductility exhaustion. The critical strain was measured as 11.5, such a high value being possible because the material was accumulating strain under high hydrostatic pressure [23].

The tests under dry conditions described above will be modelled in section 3, but in a separate set of experiments Tyfour *et al.* [24] conducted tests on BS11 rail steel under dry and wet conditions to develop the following equations, the relationship between contact conditions and the accumulated plastic shear strain  $\gamma_p$  on which the model described here is based:

$$\gamma_p = 0.00237P_r N_{\text{eff}} \quad (2)$$

$$P_r = P_{\text{eff}} - P_s \quad (3)$$

$P_r$  is the ratcheting stress,  $P_{\text{eff}}$  is the ratio of the maximum Hertzian contact pressure to the material hardness (including the effect of strain hardening) and  $P_s$  is the shakedown limit, including the effect of strain hardening and corresponding to the friction coefficient at the contact surface.  $N_{\text{eff}}$  is the number of contact cycles during which the traction coefficient exceeded 0.25. A limit of 0.25 was chosen because the distribution of shear stress below the contact (Fig. 4a) ensures that plastic flow is predominantly at the contact surface when this limit is exceeded. Full details have been given in reference [24].

## 2 EMPIRICAL RATCHETING MODEL

### 2.1 A layered representation of the rail

To model the twin-disc contact, itself representing a rail-wheel contact, a two-dimensional (i.e. line contact) half-space based model was used with an infinitely long cylinder representing the wheel disc rolling parallel to its axis on an infinitely wide plate, representing the rail disc surface. The model is shown in Fig. 5a. The pressure profile at the contact was taken to be semi-elliptical (Hertzian), and the rail half-space was divided into a series of layers of thickness  $\delta z$  parallel to the undeformed contact surface, up to a depth of approximately ten times the contact half-width. This depth is sufficient to ensure that no plastic flow took place in the deepest layer.

Contact of the wheel and rail discs produces a well-defined stress distribution local to the contact within the rail disc. The shear stress  $\tau_{zx}$  beneath a Hertzian line contact varies both with depth  $z$  and with position  $x$  ahead of and behind the contact, as shown in Fig. 4. This distribution is for a single position of the contact; however, because the wheel is passing across the rail,

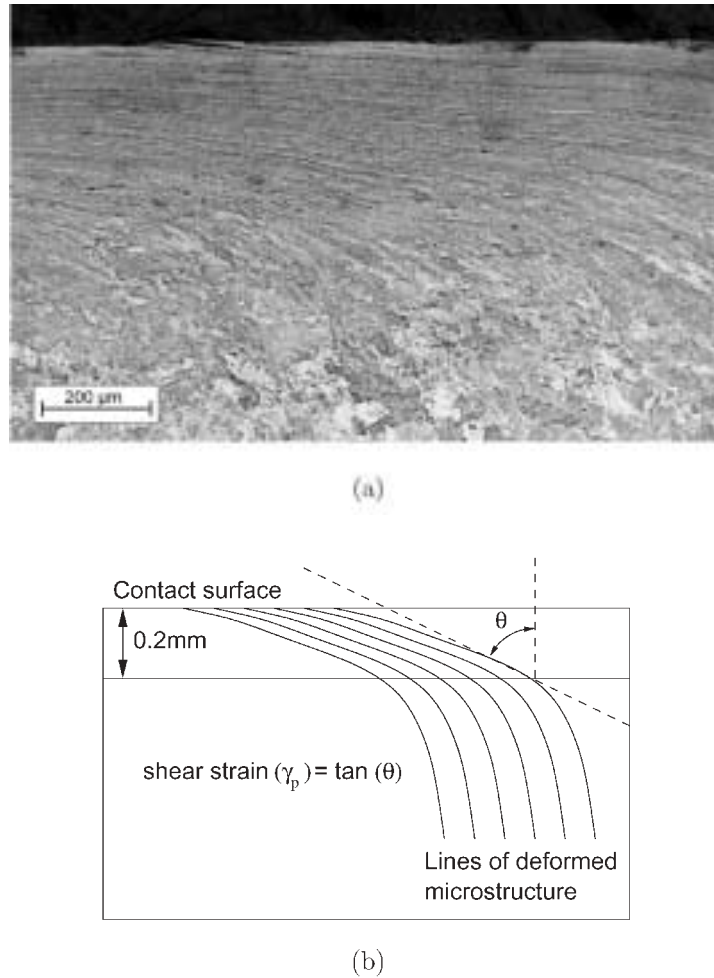


**Fig. 3** Shear strain below the rail steel surface. (a) Photograph of rail microstructure below a simulated rail-wheel contact. (b) Strain measurement technique. Deformation of the steel produces alignment of its microstructure in the direction of deformation. Measuring the angle of these deformation lines 0.2 mm below the surface gives the shear strain at this depth

all points at any particular depth in the rail disc will experience the full range of shear stress produced by the contact for any possible contact position. Although this produces a complex stress history, the material is taken only slightly above the shakedown limit in any cycle, and it is the maximum shear stress experienced by each cycle which controls ratcheting. Consequently it is possible to reduce the problem to consideration of the maximum shear stress  $\tau_{zx, \max}$  present at each depth (i.e. in each layer) during the passage of the contact.

The following equation was used to convert the shear stress  $\tau_{zx, \max}$  to a plastic shear strain increment  $\Delta\gamma_p$  per contact cycle for each layer:

$$\Delta\gamma_p = 0.00237 \left( \frac{\tau_{zx, \max}}{k_{\text{eff}, N-1}} - 1 \right) \quad (\tau_{zx, \max} \geq k_{\text{eff}, N-1}) \quad (4)$$

The quantities in equation (4) not otherwise specified are for a particular layer  $L$  and number of cycles  $N$ . This

empirical equation was developed from equation (2) and has been applied in previous ratcheting models [2, 25]. The effective shear yield stress, i.e. the shear yield stress  $k_{\text{eff}}$  following strain hardening, is a function of the current shear strain. Current shear strain cannot be known prior to the increment of strain taking place but, since the strain increments and therefore the change each cycle in  $k_{\text{eff}}$  are small, each strain increment was predicted using the value of effective shear yield stress from the previous contact cycle.  $\Delta\gamma_p$  was set to zero for cases in which  $\tau_{zx, \max} < k_{\text{eff}, N-1}$ .

To bring together the layered representation of the rail and the strain accumulation described by equation (4) a Matlab routine was written based on the flow diagram shown in Fig. 5b. Run times were of the order of a few minutes for 10–20 000 cycles on a typical desktop personal computer. The output of the model can be presented as either the predicted strain or the hardness at a particular depth below the contact surface plotted against the number of contact cycles, or as a strain or a

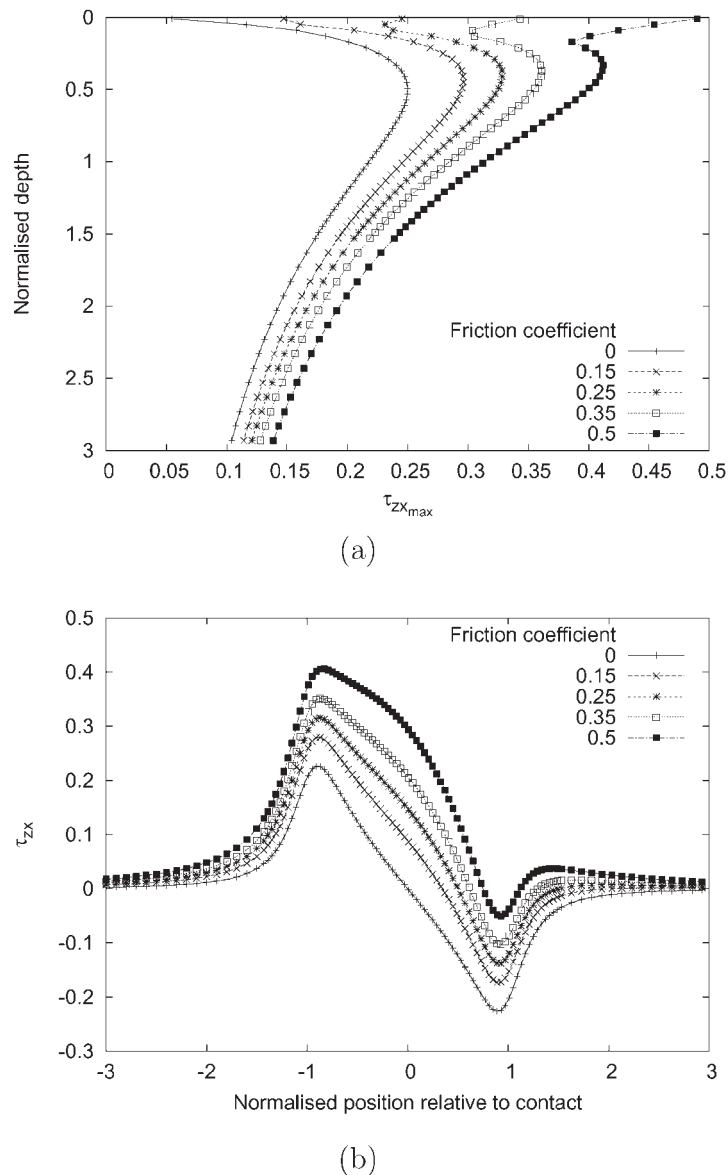


**Fig. 4** Subsurface stress beneath a Hertzian line contact. Dimensions are normalized with respect to the contact half-width for a unit maximum contact pressure. (a) Variation with depth in maximum orthogonal shear stress  $\tau_{zx,max}$  at each depth. (b) Variation in the direction of rolling of the orthogonal shear stress  $\tau_{zx}$  at a normalized depth of 0.25

hardness profile with depth for a particular number of cycles.

## 2.2 Material models

Calculation of the strain increment  $\Delta\gamma_p$  depends on the effective shear yield stress  $k_{eff}$  but this is in turn dependent on the total plastic strain  $\gamma_p$ . The stress–strain curve for the material provides the link between these quantities and, once plastic deformation is under way, it can be assumed that  $k_{eff}$  is equal to the applied shear stress  $\tau$ . The material local to the contact is highly constrained by surrounding material and it approaches a

state of hydrostatic compression under which its behaviour can be very different from that measured in a standard monotonic tensile test at atmospheric pressure [23]. However, data from standard stress–strain tests are much simpler and cheaper to obtain than are data for material under hydrostatic compression, and so there is an incentive to use them where possible.

To investigate whether standard tensile test data can be used as input to the layer-based rail–wheel simulation, three different stress–strain models (A–C) were used to provide the relationship between shear strain and shear yield stress for the deformed material. Model A was based on standard tensile test data, while models B and C were based on material behaviour under high

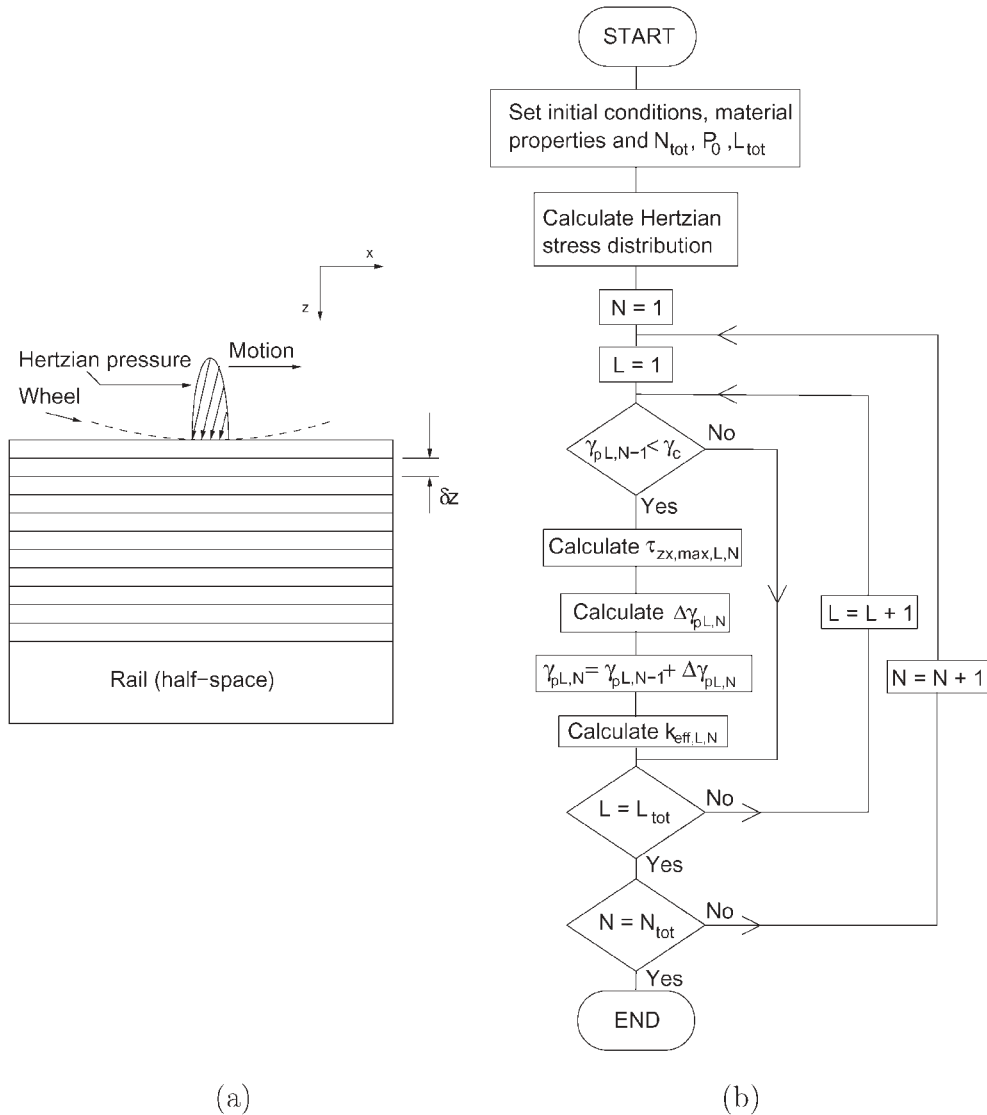


**Fig. 5** The layer model of strain accumulation and hardening. (a) Discretization of the rail half-space into layers. (b) Flow diagram for computer implementation of the model ( $N_{tot}$  is the total number of cycles to run,  $L_{tot}$  is the total number of layers in the model)

hydrostatic pressure derived from tests by Tyfour *et al.* [12]. Because material models B and C were based on the work of Tyfour *et al.* which was also to be used for validation of the layer-based model, it was important to ensure that this validation was meaningful, and this is discussed in section 3.1.

2.2.1 Materials model A

Stress-strain and strain hardening behaviour of a BS11 rail steel in uniaxial tension at atmospheric pressure is illustrated in Fig. 6a. These tensile data were converted to shear stress  $\tau$  and shear strain  $\gamma$  behaviour using the relationships given by

$$\tau = \frac{\sigma}{\sqrt{3}} \tag{5}$$

$$\gamma = \sqrt{3}\epsilon \tag{6}$$

where  $\sigma$  and  $\epsilon$  are the tensile stress and strain respectively.

To represent the plastic shear strain  $\gamma_p$  data mathematically for the input to the layer model, a modified Voce equation was used with the form

$$\tau = m(1 - e^{-n(\gamma_p)})^p \tag{7}$$

The elastic yield strain was subtracted from the strain data prior to fitting this equation to the post-yield test results, giving constants  $m$ ,  $n$  and  $p$  of 572, 0.8 and 0.3 respectively. Because the decrease in stress observed in the test data for tensile strains above 0.15 was the result of necking in the specimen, the tensile stress was

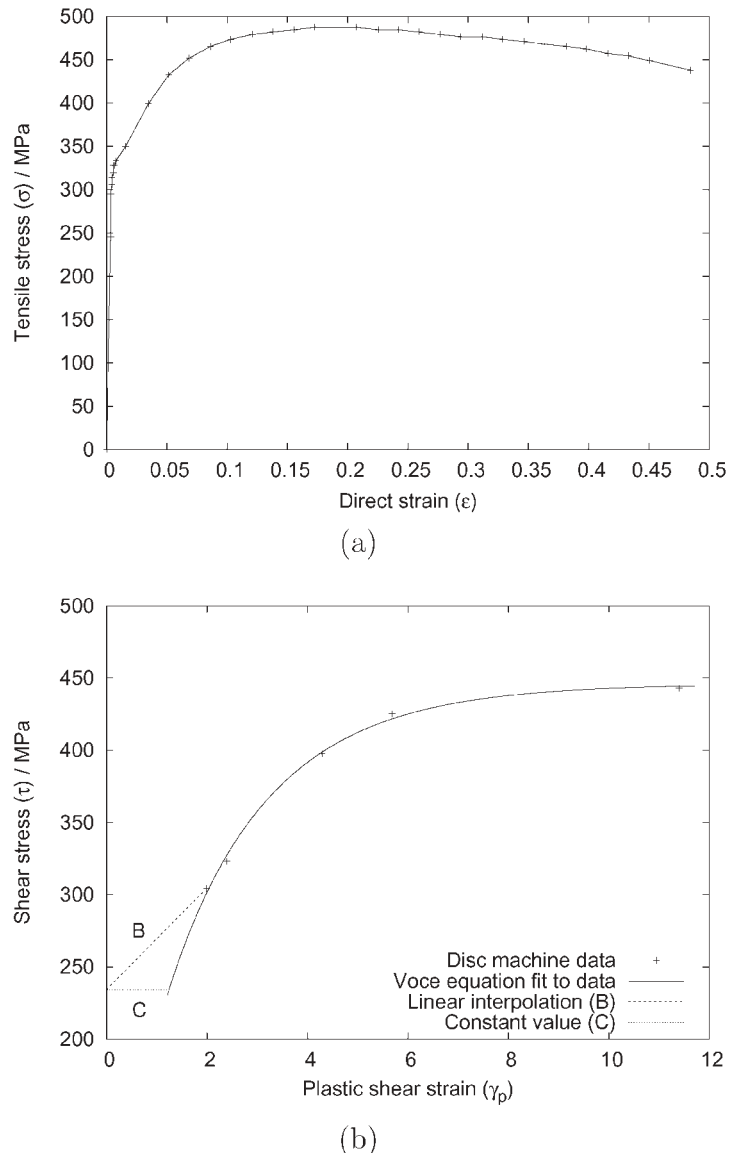


**Fig. 6** Stress–strain behaviour for BS11 rail steel. (a) Tensile data generated at atmospheric pressure using a tensile test. (b) Shear data derived from twin-disc tests for material under a high hydrostatic pressure. Curves B and C define behaviour at low strains for which no experimental data were available

assumed to remain constant at 490 MPa for strains exceeding this value.

### 2.2.2 Materials model B

Following rolling–sliding contact twin-disc tests over a range of distances, Tyfour *et al.* [12] measured both the accumulated plastic strain and the percentage hardening 0.2 mm below the test disc surfaces. If it is assumed that the measured percentage hardening is proportional to the percentage increase in shear yield stress [26], then the data can be used to construct the stress–strain curve for BS11 rail steel undergoing rolling–sliding contact at a high hydrostatic pressure, and this is shown in Fig. 6b. Above a shear strain of 2 the stress–strain

behaviour is relatively well defined and can be represented using a Voce equation of the form given by equation (7) with coefficients  $m$ ,  $n$  and  $p$  of 446, 0.47 and 0.80 respectively. However, there is considerable uncertainty about the behaviour of the material at low strains.

To provide a stress–strain relationship for low strains the initial shear yield stress of the material prior to plastic deformation (234.4 MPa) can be used to give a data point at zero plastic strain, and linear interpolation between this point and the first known data point can then be used to construct the curve. Material B was therefore defined using the combination of a linear relationship at low strains and the Voce-type relationship at strains above 2. A plot of this material behaviour is shown in Fig. 6b, curve B.

### 2.2.3 Materials model C

Material model C was based on data identical with those for model B, but the assumption about behaviour at low strains is different. For material model C it was assumed that shear yield stress was constant at 234.4 MPa (the initial yield point of the unstrained material) until the value predicted by the Voce equation fit to the experimental data exceeded this level. This is shown as curve C in Fig. 6b.

## 2.3 Variable-friction loading

In general, rail–wheel contact takes place at a variety of surface friction levels, depending on the environmental conditions. For example, water reduces the rail surface friction coefficient to around half its value under dry conditions, when it is typically in the range 0.2–0.6.

Two alternative methods were developed for including friction variation in the layer model. These were investigated by modelling the friction variation observed in the tests conducted by Tyfour *et al.* [12], shown in Fig. 2. Firstly, an upper-bound–lower-bound approach was used in which two runs of the model were made for comparison of the high and low extremes of friction coefficient observed. In the second, more sophisticated approach, the observed friction history was divided into a series of ‘blocks’ of uniform friction coefficient. These were then applied to the modelled material sequentially in a single run of the layer model to examine their compound effect. A cycle-by-cycle variation in friction coefficient was not applied because it would be unrealistic to use such a method in a railway environment, for which it is difficult to record data over a long period.

Normal loads can also vary, depending on, for example, vehicle type. Variation in normal load is not investigated here but could be tackled using the same approaches as are described for surface friction.

## 3 TEST PROGRAMME

The simulations conducted are summarized in Table 1. For each simulation the maximum Hertzian contact pressure was 1500 MPa, a contact half-width of

**Table 1** Test programme

Simulation	Material model	Friction
1	A	Upper–lower bound
2	B	Upper–lower bound
3	C	Upper–lower bound
4	C	1000 cycles high friction; 39 000 cycles low friction
5	C	4000 cycles high friction; 36 000 cycles low friction

0.31 mm was used, and 40 000 contact cycles were simulated. These conditions correspond to those used by Tyfour *et al.* [12] in the experiments described in section 1.3. A single-layer thickness  $\delta z$  of 0.05 mm was used, with 60 layers giving the simulations a depth of 3 mm. For tests with upper and lower friction coefficient boundaries, these were set at 0.44 and 0.27 respectively, again to correspond to those measured by Tyfour *et al.* [12].

## 3.1 Validation

For material model A, validation was by comparison of the modelling results with experimental data from Tyfour *et al.* [12] on the variations in shear strain and percentage hardening with the number of contact cycles for a depth 0.2 mm below the contact surface. For material models B and C such a comparison would have been unsatisfactory because these experimental data had formed an input to the models. To overcome this problem an alternative validation technique was developed using data collected by Tyfour *et al.* [12] on the variation in hardness with depth at particular numbers of contact cycles. This comparison provided a means to validate and check the output of the layer model using data which had not formed an input to it. Results of this validation are presented for simulation 4 but could equally have been presented for any of the simulations using material models B or C because these material models were very similar.

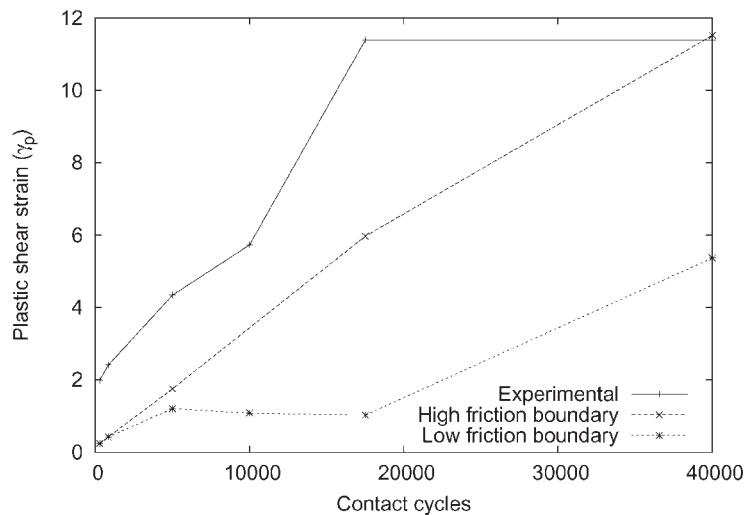
## 4 RESULTS

### 4.1 Simulation 1

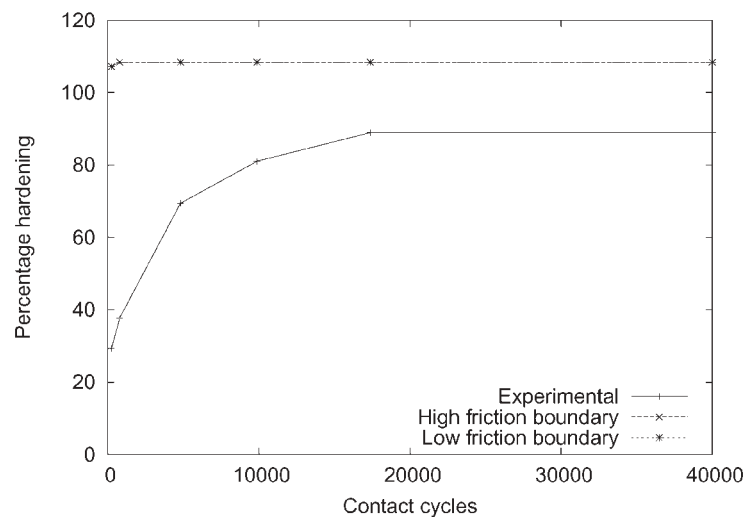
Simulation 1, based on material model A (monotonic tensile data), gave results which indicated less rapid strain accumulation and more rapid hardening than was observed experimentally. Figures 7a and b show the evolution behaviours of plastic shear strain and percentage hardening respectively at a depth 0.2 mm below the contact surface for both the simulation and the corresponding experiments. The hardening results for the upper- and lower-bound friction coefficients were almost indistinguishable.

The simultaneous presence of more rapid hardening and a less rapid accumulation of plastic shear strain than seen experimentally is to be expected from equation (4), which shows that the plastic strain increment is linked to the ratio of  $\tau_{zx, \max}$  to  $k_{\text{eff}}$ . Because material model A predicts very rapid hardening relative to material under high hydrostatic pressure,  $k_{\text{eff}}$  rises early in the simulation, and the ratio of  $\tau_{zx, \max}$  to  $k_{\text{eff}}$  falls, causing reduced plastic strain increments in subsequent cycles.

For the upper-bound case (high friction coefficient) the strain at the end of the simulation and the strain at the



(a)



(b)

**Fig. 7** Results for simulation 1 at a depth 0.2mm below the contact surface, plotted with comparable experimental results: (a) plastic shear strain accumulation, (b) percentage hardening

end of the experiment are almost identical, but the strain is consistently under-predicted throughout the simulation up to this point. For the lower-bound case the strain is also under-predicted, but it remains at around half the experimental value at the end of the simulation. However, although the upper-bound simulation and experimental values of accumulated strain agree at 40 000 cycles, this does not indicate success in the simulation process; it is simply a consequence of the gradual accumulation of strain up to the limiting value  $\gamma_c$ .

#### 4.2 Simulation 2

Results from simulation 2, based on material model B (stress-strain data generated under a high hydrostatic

pressure) show a marked improvement in their agreement with experimental results over those from simulation 1.

Figures 8a and b illustrate the accumulation of plastic strain and the hardening behaviour respectively over 40 000 contact cycles. At low numbers of contact cycles (less than 10 000), results from both high- and low-friction-coefficient boundaries are similar, and both are in good agreement with the experimental measurements of strain and hardening. At higher numbers of contact cycles the predictions based on the upper bound of the friction coefficient are in better agreement with the experimental data. By 40 000 cycles the predicted hardness has become almost identical with the observed experimental values; however, strain accumulation shows a rising trend, indicating that the predicted rate

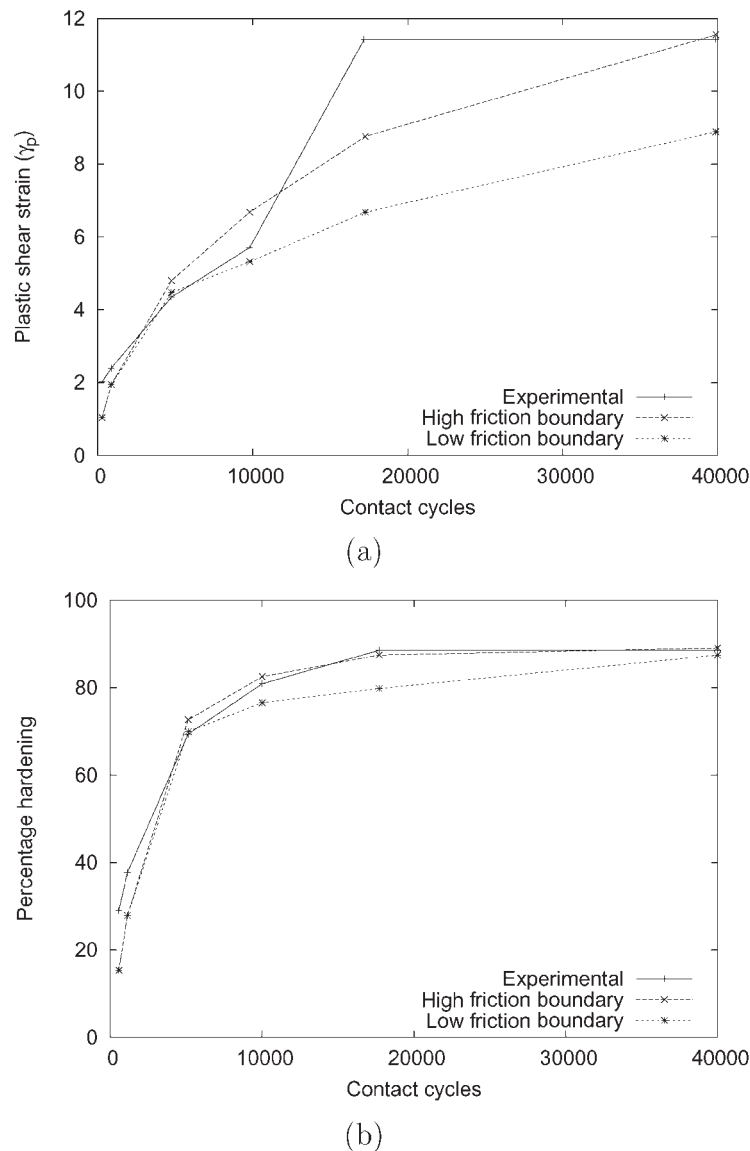


**Fig. 8** Results for simulation 2 at a depth 0.2mm below the contact surface, plotted with comparable experimental results: (a) plastic strain accumulation, (b) percentage hardening

of strain accumulation lags behind the rate measured in the experiments.

### 4.3 Simulation 3

Simulation 3 was based on material model C (a variation of the interpretation of the high-hydrostatic-pressure stress-strain data). Results showed further improvement over simulation 2, particularly in the rate of strain accumulation. Figures 9a and b illustrate the results for plastic strain accumulation and percentage hardening respectively together with experimental results.

Results for both upper- and lower-bound friction coefficients were similar in the earliest cycles (up to 5000 cycles), showing similarity to the trend observed in simulation 2. At higher numbers of cycles the

upper-bound friction coefficient gave, as would be expected, more rapid strain accumulation and hardening than did the lower bound. Although the upper-bound condition leads to initial over-prediction of accumulated shear strain, the number of cycles at which the failure strain of 11.5 is reached is in good agreement with the experimental results. Agreement is less good for the lower-bound results, but even here the gradient of the shear strain curve in the 20 000–40 000 cycle period is reduced below that in simulations 1 and 2.

### 4.4 Simulations 4 and 5

Simulations 4 and 5 used material model C together with a block loading approach to represent the variation in the friction coefficient observed by Tyfour *et al.* [12]

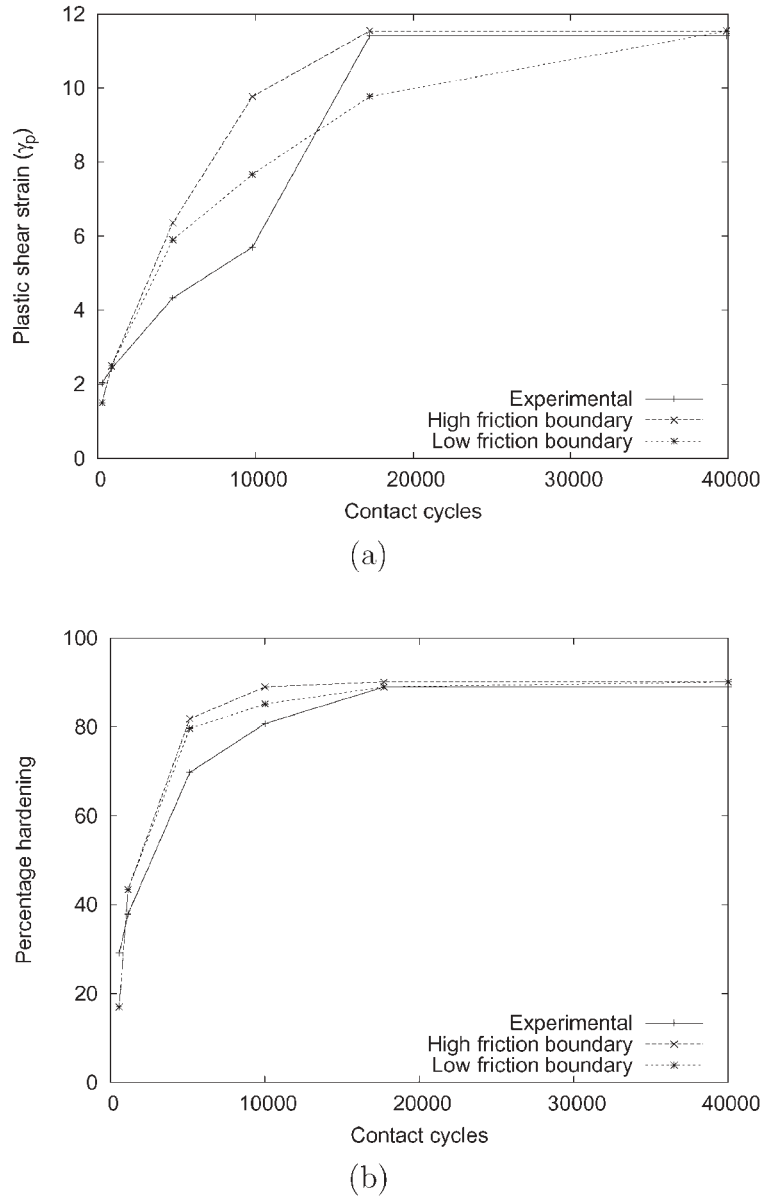


**Fig. 9** Results for simulation 3 at a depth 0.2mm below the contact surface, plotted with comparable experimental results: (a) plastic strain accumulation, (b) percentage hardening

(Fig. 2). The simulations differed in the length of the initial high-friction period of loading (1000 and 4000 cycles respectively for simulations 4 and 5) but results were almost identical for both.

Figures 10a and b present results for plastic strain accumulation and percentage hardening respectively from simulation 4. For both strain accumulation and hardening results, the fit between the predictions of the model and the experimental results is very good. However, as discussed in section 3.1, because the experimental data on hardening and deformation 0.2mm below the contact surface formed an input to the model, this quality of fit cannot be relied upon as

an indicator of the validity of the model. Figure 10c allows this problem to be overcome by presenting the variation in hardness with depth below the contact surface predicted by the simulation, together with experimental data. These experimental data did not form an input to the model, but a good fit is found between the output of the model and the experimental data at both 1000 and 17500 contact cycles, indicating the validity of the model. Tyfour *et al.* reported difficulties in accurately measuring the microhardness of the rail material very close to the disc surface, and it is therefore not possible to evaluate the performance of the simulation in the region above 0.1 mm.

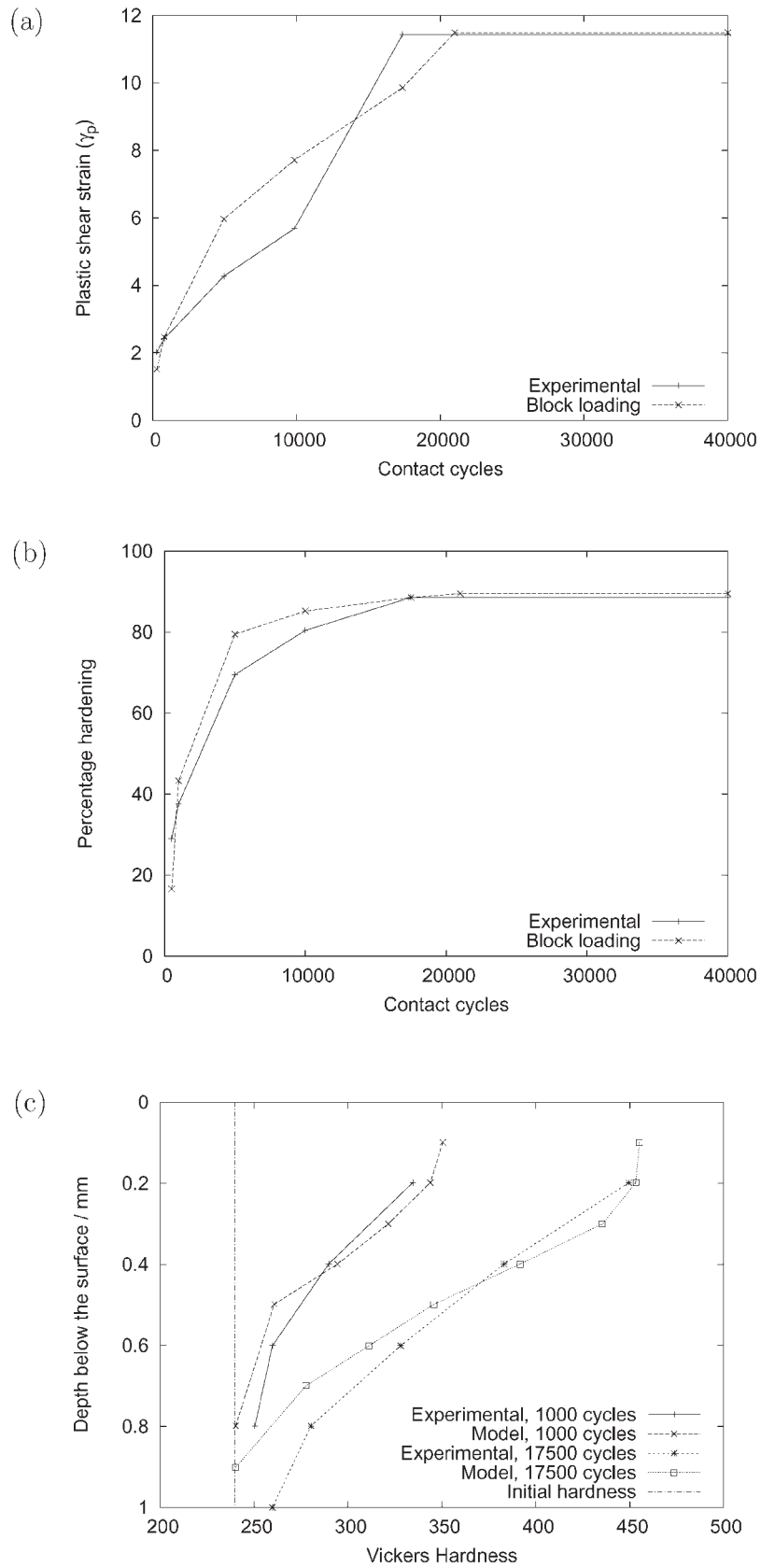


**Fig. 10** Results for simulation 4, plotted with comparable experimental results. (a) Plastic strain accumulation 0.2 mm below the contact surface. (b) Percentage hardening 0.2 mm below the contact surface. (c) Variation with depth in the Vickers hardness calculated from percentage hardening results and a core hardness of 240 HV

## 5 DISCUSSION

### 5.1 Material model

Comparison of the stress–strain curves for BS11 rail steel at atmospheric pressure and at a high hydrostatic pressure (Fig. 6) illustrates the difference between the material behaviours of these conditions. Since high-hydrostatic-pressure conditions exist in rolling–sliding contact, it is unsurprising that simulation 1, based on material model A, gave results which were significantly different from, and less realistic than, those based on material models B and C. This indicates that the tensile test data generated at atmospheric pressure on which material model A was based were not sufficient to model the strain hardening and strain accumulation that take place under a high hydrostatic pressure. However, although the results of simulation 1 were inexact, the trends predicted in behaviour were correct. In particular, the predicted plastic strain showed the expected dependence on friction.

Material models B and C gave very similar results, the differences between them being slight relative to the difference from material model A. While model C was thought to give marginally better simulation results and was used for the examination of block loading in simulations 4 and 5, these results indicate that a well-defined stress–strain curve generated under a high hydrostatic pressure is the key to successfully modelling rail–wheel contact.

### 5.2 Variable-friction loading

Comparison of results from simulations 3, 4 and 5 (Figs 9 and 10) indicates that ‘block loading’ to represent the actual friction levels to which a material is subjected during use gives results which more closely approach the experimental data than when using the upper- and lower-bound approach for varying friction. Of the upper- and lower-bound results it is the upper-bound results that most closely approximate the experimental data. This indicates that, in the short term (i.e. until the affected material is worn away), behaviour of the material is influenced primarily by the highest friction levels to which it is subjected, even if the high friction acts for only a small proportion of the contact cycles. Figure 2 indicates that, for the tests by Tyfour *et al.* [12], friction was at its highest during the first 5000 cycles of the 40 000 cycle test.

The limit of the influence of a brief high-traction period will be when the upper layers of material reach failure and are removed as wear debris. Lower layers which are revealed by this wear, and which were sufficiently deep to have been untouched by the high-traction period, may then be more exactly modelled using a lower friction coefficient. (Figure 4a indicates the depths at

which stresses due to various traction coefficients have the greatest influence.) In the current simulations, removal of failed layers is not implemented; however, experimental measurements of wear indicate that over 40 000 cycles the disc would have lost only 0.2 mm from its surface. Therefore, even if this depth of material were removed, the material revealed would still have been influenced by the initial high-traction period. Consequently, the high-traction boundary gave the best approximation to the experimental data. In a future implementation of the model, the removal of failed layers will be included to improve the response of the model to variations in friction, including friction ‘histories’ much more complex than those currently considered.

## 6 CONCLUSIONS

A model has been developed to investigate plastic strain accumulation in a railway rail steel subjected to repeated contact leading to ratcheting, a process that may precede later wear or the initiation of rolling contact fatigue cracks. Tens of thousands of contact cycles can be simulated in a few minutes using a personal computer. Validation using data from small-scale twin-disc rolling–sliding contact tests on a rail steel indicates that the model can successfully predict rail steel strain accumulation and hardening when using a material model based on stress–strain behaviour of rail steel under high hydrostatic compression. A material model based on data obtained at atmospheric pressure was successful in predicting trends in strain accumulation and hardening, but not their rates. Results from the model were improved by considering the surface friction history to which the rail steel was subjected, rather than by considering only the upper and lower boundary values of friction. In further development of the model, the effect of surface wear of the rail steel on its hardening and accumulated strain will be considered.

## ACKNOWLEDGEMENTS

This project was financially supported by the European Union through the Brite Euram project ICON [27].

## REFERENCES

- 1 Plummer, P. (Ed.) Network Rail 2003 technical plan. Technical Report, Network Rail, London, 2003.
- 2 Kapoor, A. and Franklin, F. J. Tribological layers and the wear of ductile materials. *Wear*, 2000, **245**, 204–215.
- 3 Fletcher, D. I., Franklin, F. J. and Kapoor, A. Image analysis to reveal crack development using a computer simulation of wear and rolling contact fatigue. *Fatigue Fracture Engng Mater. Structs*, 2003, **26**(10), 957–967.

- 4 Kapoor, A., Schmid, F. and Fletcher D. I. Managing the critical wheel/rail interface. *Railway Gaz. Int.*, January 2002, **158**(1), 25–28.
- 5 Kapoor, A. Wear fatigue interaction and maintenance strategies. In *Why Failures Occur in the Wheel Rail System*, Derby, 2001 (Advanced Railway Research Centre, The University of Sheffield, Sheffield).
- 6 Armstrong, P. J. and Frederick, C. O. A mathematical representation of the multiaxial bauschinger effect. Technical Report RDBN731, Central Electricity Generating Board, 1966.
- 7 Jiang, Y. and Sehitoglu, H. Modelling cyclic ratcheting plasticity, part i: development of constitutive relations. *Trans. ASME, J. Appl. Mechanics*, 1996, **63**, 720–725.
- 8 Jiang, Y. and Sehitoglu, H. Modelling cyclic ratcheting plasticity, part ii: comparison of model simulations with experiments. *Trans. ASME, J. Appl. Mechanics*, 1996, **63**, 726–733.
- 9 Lemaitre, J. and Chaboche, J.-L. *Mechanics of Solid Materials*, 1990 (Cambridge University Press, Cambridge).
- 10 Ringsberg, J. W., Bjarnehed, H., Johansson, A. and Josefson, B. L. Rolling contact fatigue of rails—finite element modelling of residual stresses, strains and crack initiation. *Proc. Instn Mech. Engrs, Part F: J. Rail and Rapid Transit*, 2000, **214**(F1), 7–19.
- 11 Ringsberg, J. W., Loo-Morrey, M., Josefson, B. L., Kapoor, A. and Beynon, J. H. Prediction of fatigue crack initiation for rolling contact fatigue. *Int. J. Fatigue*, 2000, **22**, 205–215.
- 12 Tyfour, W. R., Beynon, J. H. and Kapoor, A. The steady state wear behaviour of pearlitic rail steel under dry rolling–sliding contact conditions. *Wear*, 1995, **180**, 79–89.
- 13 Nielsen, J. C. O. and Stensson, A. Enhancing freight railways for 30 tonne axle loads. *Proc. Instn Mech. Engrs, Part F: J. Rail and Rapid Transit*, 1999, **213**(F4), 255–263.
- 14 Hertz, H. On the contact of elastic solids. In *Miscellaneous Papers by H. Hertz*, 1896, pp. 146–183 (Macmillan, London).
- 15 Kalousek, J. Wear and contact fatigue model for railway rail. Technical Report 1986/10, National Research Council, Canada, 1986.
- 16 Beagley, T. M., McEwan, I. J. and Pritchard, C. Wheel/rail adhesion—boundary lubrication by oily fluids. *Wear*, 1975, **31**, 77–88.
- 17 Beagley, T. M. and Pritchard, C. Wheel/rail adhesion—the overriding influence of water. *Wear*, 1975, **35**, 299–313.
- 18 Kapoor, A. A re-evaluation of the life to rupture of ductile metals by cyclic plastic strain. *Fatigue Fracture Engng Mater. Structs*, 1994, **17**(2), 201–219.
- 19 Tyfour, W. R. and Beynon, J. H. The effect of rolling direction reversal on fatigue crack morphology and propagation. *Tribology Int.*, 1994, **27**, 401–412.
- 20 Garnham, J. E. and Beynon, J. H. The early detection of rolling–sliding contact fatigue cracks. *Wear*, 1991, **144**, 103–116.
- 21 Fletcher, D. I. and Beynon, J. H. Development of a machine for closely controlled rolling contact fatigue and wear testing. *Trans. ASME, J. Test. Evaluation*, 2000, **28**(4), 267–275.
- 22 Bower, A. F. The influence of crack face friction and trapped fluid on rolling contact fatigue cracks. *Trans. ASME, J. Tribology*, 1988, **110**, 704–711.
- 23 Pugh, H. L. D. *Mechanical Behaviour of Materials under Pressure*, 1970 (Elsevier, Amsterdam).
- 24 Tyfour, W. R., Beynon, J. H. and Kapoor, A. Deterioration of the rolling contact fatigue life of pearlitic rail steel due to dry–wet rolling–sliding line contact. *Wear*, 1996, **197**, 255–265.
- 25 Kapoor, A. Mechanics of failure in a hardening and wearing surface. In *The Mechanics and Materials Science of Contact: Issues and Opportunities*, Report 94-17, Vanderbilt University, Nashville, USA, Institute of Mechanics and Materials, University of California, San Diego, La Jolla, California, USA, July 1994.
- 26 Cahoon, J. B., Broughton, W. H. and Kutzak, A. R. Determination of yield strength from hardness measurements. *Metall. Trans.*, 1971, **2**, 1979–1983.
- 27 ICON: integrated study of rolling contact fatigue. European Union Brite-EuRam III project BRPR960245, 1997–1999.